Journal of Machine Engineering, 2023, Vol. 23, No. 2, 41–65
ISSN 1895-7595 (Print) ISSN 2391-8071 (Online)

Received: *12 February 2023* / Accepted: *22 March 2023* / Published online: *24 March 2023*

force transducer optimization,
stationary dynamometer,
cutting force measurement

Muhammad RIZAL[1*], Jaharah A. GHANI[2]
Husni USMAN[1], Muhammad DIRHAMSYAH[1]
Amir Zaki MUBARAK[1]

DESIGN AND OPTIMIZATION OF A CROSS-BEAM FORCE TRANSDUCER FOR A STATIONARY DYNAMOMETER FOR MEASURING MILLING CUTTING FORCE

This paper's objective is to design and optimize a force transducer to build a stationary dynamometer that can measure three axes of milling cutting force. To reduce interference error and increase sensitivity, the force transducer's Maltese cross-beam design was optimized. The force transducer's performance depends on three design parameters: the cross-rectangular beam's through-hole length and width, the compliant plate thickness, and the strain, stress, and stiffness of force transducer constructions calculated by ANSYS. The response surface method (RSM) estimates a desired second-order polynomial function for three geometric parameters based on sensitivity, interference error, safety factor, and stiffness. A stationary dynamometer prototype was made with four optimized force transducers and several piezoresistive strain sensors. The developed dynamometer has good linearity, repeatability, and hysteresis, as well as high sensitivities and low cross-sensitivity errors. The reference dynamometer's cutting force measurements were very close to those of the designed dynamometer in the validation test.

1. INTRODUCTION

Important aspects in the manufacturing industries are ensuring product quality and variable product dimensions. Because of this, it is important to have an online tool condition monitoring (TCM) system that can continuously monitor certain parameters to ensure the cutting tool and the process are in excellent condition [1]. This is consistent with Industry 4.0 frameworks, which include data collection as a component of real-time monitoring and smart evaluation. Cutting conditions include cutting speed, feed rate, depth of cut, cutting tool shape, cooling technique, and workpiece and tool materials that may significantly influence the cutting force [2]. Therefore, it is employed as a significant indicator for the optimization of machining parameters and the machinability studies of hard materials [3, 4]. Even with

[1] Department of Mechanical Engineering, Faculty of Engineering, Syiah Kuala University (USK), Indonesia
[2] Department of Mechanical and Manufacturing Engineering, Faculty of Engineering and Built Environment, University Kebangsaan Malaysia (UKM), Malaysia
[*] E-mail: muh.rizal@usk.ac.id
https://doi.org/10.36897/jme/162514

minor variations in tool wear, surface roughness, vibration, and chatter, the cutting force reflects the machining conditions. Hence, measuring the cutting force is an impressive way for machining condition monitoring, such as tool wear monitoring [5] and tool breakage detection [6], and it may give data support for the research of cutting tool performance [7], tool life [8], and chatter investigations [9, 10]. To better accommodate the cutting force measurement system, many different types of dynamometers, each with its own unique design and technique of measurement methods, have been developed.

Researchers in the past have attempted to address the demand for a reliable cutting force measurement system by introducing various designs, methods, and dynamometer configurations. Byrne et al. [11] and Totis et al. [12] constructed rotating dynamometers for monitoring cutting forces in milling and drilling processes using piezoelectric sensors. Rizal et al. [8] have developed a rotating dynamometer that measures the primary and perpendicular cutting forces, as well as the thrust force, using metal foil strain gauges attached to a cross-beam force transducer mounted on a conventional milling tool holder. Qin et al. [13] also proposed employing semiconductor strain gauges on a thin structure, like the lantern shape on the milling tool holder, to measure the thrust force and torque. Furthermore, the rotating dynamometer employs capacitive sensors [14], fiber Bragg grating sensors on the semi-octagonal rings [15], and polyvinylidene fluoride (PVDF) sensors [16]. Principally, these techniques combine sensors on a rotating tool holder that has been adapted to accommodate their modules and instruments. The rigidity of the tool holder and the natural frequency of the construction will drop by 45 % [17]. According to earlier work conducted by Rizal et al. [18], Xie et al. [14], and Qin et al. [19], the integrated rotating dynamometer's natural frequencies only reached the ranges of 400–470 Hz and 608–640 Hz. Consequently, the application range of these dynamometers is restricted to low and medium spindle speeds. In addition, the installation of wireless devices atop a spinning tool holder provides inertial force due to the instrumentation's weight. It will interfere with the output signal and increase the output measurements' uncertainty.

The second kind of dynamometer is the piezoelectric element–based table dynamometer, which is widely utilized in academic machining processes because of its high sensitivity, high bandwidth, and reliability [20]. However, some of the issues with piezo-electric sensors include low spatial resolution and charge leakages [2], voltage degradation or drifts in the presence of static pressures, and the high cost of the sensors themselves. On the other hand, commercial piezoelectric-based dynamometers are expensive due to their sophisticated design and the need for extra charge amplifiers and associated wiring. The cutting force measuring system's cost-effectiveness is a further key requirement for sensor application in automation and real-time condition monitoring in the manufacturing sectors. These factors have motivated researchers to create alternatives, such as stationary or table dynamometers. Subasi et al. [21] developed a milling process table dynamometer using photo-interrupters. Adopting the folded leaf spring, they utilized optoelectronic sensors capable of detecting the displacement of a flexural component. Light interruption between an optically connected LED and a light-receiving transistor converts linear displacement into an output voltage. However, they only employed a single flexural component, which would lead to top plate deformation at the precise instant when the thrust force of the cutting tool moves away from the dynamometer's centre. Gomez and Schmitz [22] also developed a milling

dynamometer that uses the flexure-based kinematics or constrained motion method, in which force is inferred from displacement measured by an optical interrupter. By inverting the frequency response function (FRF) from the measured displacement, they determined the cutting force in the time domain using a structural deconvolution technique. Similarly, Sandwell et al. [23] employed an optical sensor to measure the horizontal cutting forces and torque on the table dynamometer. In order to boost their sensitivity, optical sensors require large structural deformations. More deformation, however, diminishes the structure's stiffness and resonance frequency. Therefore, the transmissibility of the dynamometer will be limited to a frequency range between 600 and 700 Hz [21, 22].

Measuring the cutting force can also be done by detecting the surface strain of dynamometer structures. Table dynamometers with polyvinylidene fluoride (PVDF) thin-film sensors were proposed by Luo et al. [16]. There are six sensors strategically placed around the table to measure pressure in all three dimensions. Li et al. [24] developed a strain-type, three-component table dynamometer by mounting a strain gauge on eight parallel elastic beams. These beams were deployed to increase the stiffness, and the construction of the vertical beam was adjusted to minimize the effect of eccentric force on the measurement result. Yaldiz et al. [25], Mohanraj et al. [26], and Alipanahi et al. [27] also proposed the table dynamometer utilizing a metal foil strain gauge set on four octagonal rings force transducers. However, four transducers were required to sustain the dynamometer's top plate. Due to the fact that the octagonal ring structure had only two directions of force, sensor readings were inconsistent.

Designing a force transducer for dynamometer requires careful consideration of a number of factors, including the geometry of the force transducer structure and the type of sensor used, both of which have a significant impact on the transducer's rigidity and its capacity to withstand dynamic loads. It is crucial to select the appropriate sensor type for a dynamometer, as most of the previously reported dynamometers use metal-based strain gauge sensors with low gauge factors compared to semiconductor or piezoresistive types with gauge factors that may approach 100–150 [28]. Furthermore, dynamometers are being developed to measure forces along all three axes with minimal crosstalk between channels. The degree of cross-talk error can be minimized while the transducer's structural rigidity is preserved by optimizing the geometry of the transducer's supporting structure. Li et al. [29] has implemented an optimization approach in order to minimize the interference error that occurs on the wheel force transducer structure. They optimized the four parameters of the "T"-shaped dimension of the structure, which resulted in a decrease in interference error from 42.71% to 8.76%. However, it is rare for force transducers for cutting force measuring dynamometers to be designed with structural optimization in mind, despite the fact that this process is important to developing a precise measurement.

In this work, we propose a novel cross-beam force transducer for constructing a stationary dynamometer that was optimized using response surface methodology (RSM). A stationary dynamometer prototype was constructed with four optimized force transducer structures and a number of piezoresistive strain sensors. A series of calibration tests were performed to determine sensitivity, linearity, hysteresis, and repeatability. The actual milling tests were also conducted to examine the functionality of the dynamometer for milling applications.

2. CROSS-BEAM FORCE TRANSDUCER

2.1. GEOMETRY OF FORCE TRANSDUCER

The ability to detect forces in three-axis directions within one compact structure, possessing self-decoupling capabilities, and having appropriate rigidity are all important factors to take into account when designing force sensors. Fig. 1a illustrates the proposed geometry and shape of the cross-beam force transducer. The geometric design consisted of a slotted cross-beam that was able to detect forces along three axes, such as the *x*-axis, the *y*-axis, and the *z*-axis. The main parts of the force transducer geometry included an elastic cross-beam with squared through holes (1–4) connected from the compliant plates (5) to the central hub (6) as shown in Fig. 1b. Each beam had vertically squared through holes (7–10) and horizontally squared through holes (11–14) perpendicular to each other to increase sensitivity and decoupling. The forces or loads were transmitted by the central hub (6) to the four beams and compliant plates such that they ended in the bottom ring plate (15), which was fixed. In order to reduce the effects of stress concentration on the structure, all edges and the transition zone from the beams to the central hub were filleted.

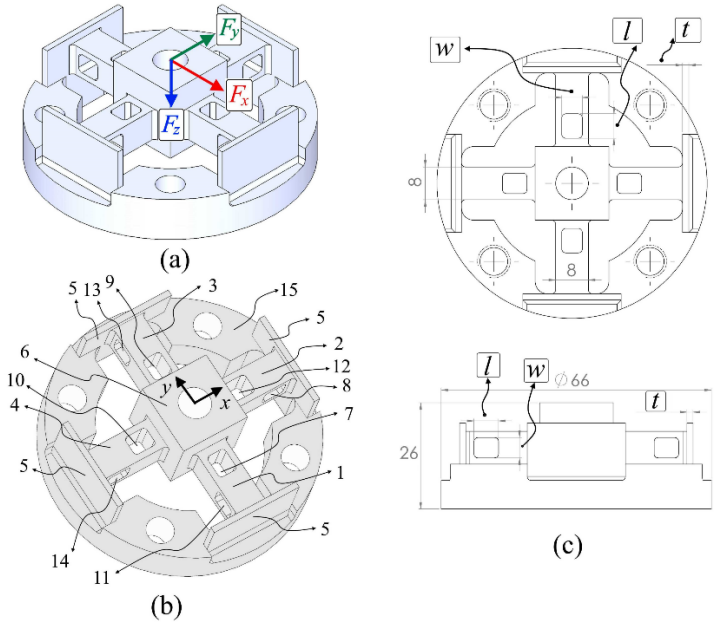

Fig. 1. Geometry of the cross-beam force transducer

As illustrated in Fig. 1c, the cross-beam force transducer had the following dimensions: 66 mm in diameter, and 26 mm in height, and the cross-sectional size of the beam was 8×8 mm. The design variables for the force transducer are *w* (mm) and *l* (mm), which represent the width and length of the rectangular through holes in the beam, respectively, while *t* (mm) represents the variable thickness of the compliant plate.

The force transducer was designed in a significantly different way from a standard Maltese cross-beam. All forces and moments can be detected with the use of the classic Maltese cross-beam, which consists of a central hub and four solid beams. Whereas this force transducer has four beams connected to a central hub to detect F_x, F_y, and F_z. Each beam comprised eight rectangular through-holes, which had the benefit of focusing the strain on the surface of the cross-beam, hence improving the sensor's sensitivity. Four vertical through-holes increased the sensitivity of the horizontal forces F_x and F_y, whereas four horizontal through-holes detected the F_z force. Furthermore, each end of the beam was attached to the solid rim by a compliant plate, which separated the elastic body or sensing element from the solid load transmission element. It was capable of effectively reducing interface errors and increasing force sensor sensitivity.

2.2. DESIGN OF EXPERIMENT

In order to obtain the best performance of dynamometer, the geometry parameters of the force transducer element were optimized using response surface method (RSM). The proposed force transducer had been based on the concept of the Maltese cross-beam which is improvised and modified to enhance sensitivity as well as to minimize interference error or cross-talk error. Thus, various dimensional parameters, such as length and width of rectangular through-hole in the beam as well as compliant plate thickness, had been identified as essential parameter design. Because the piezoresistive strain sensor had been mounted on a plane surface perpendicular to the rectangular through-hole in the direction parallel to the cross-beam, the sensitivity of the sensor had been increased but error interference had been reduced. As a result, the three geometry parameters in the force sensor structure were critical and needed to be optimized in order to improve sensitivity and strength, minimize cross-talk error and maximize rigidity. The parameters and correspond-ding levels of the force transducer have been listed in Table. 1. In this study, the central composite design (CCD) was selected so as to optimize the compositional parameters and to estimate quadratic effects of through-hole width, w (mm), through-hole length, l (mm) and thickness of compliant plate, t (mm).

Table 1. Force transducer design parameters and their levels

Symbol	Factor	Unit	Level	
			Low (–1)	High (+1)
A	Through-hole width (w)	mm	3	6
B	Through-hole length (l)	mm	3	8
C	Thickness of compliant plate (t)	mm	1	3

Eighteen experiments with the four centre points were performance by selection of three factors: through-hole width (A), through-hole length (B) and thickness of compliant plate (C). Each parameter of A, B and C had two levels, low (–1) and high (+1), that were 3 and 6 mm, 3 and 8 mm, as well as 1 and 3 mm respectively.

2.3. FINITE ELEMENT METHOD

Finite element analysis was used to analyse the force transducer structure of the constructed orthogonal array shown in Table 2. The material aluminum alloy 5083-H112 was chosen due to its lightweight and good corrosion resistance with its density of 2600 kg/m^3, Young's modulus of 70.3 GPa, Poisson ratio of 0.33, and yield strength of 190 MPa. The analysis of the force transducer was performed using ANSYS to obtain stress, strain, and deformation when the structure was subjected to an external load of 500 N.

Table 2. Variation of test run values of different parameter designs

No. of Test Run	Geometry parameters		
	Through-hole width, *w* (mm)	Through-hole length, *l* (mm)	Thickness of compliant plate, *t* (mm)
1	6	3	3
2	4.5	8	2
3	6	5.5	2
4	4.5	5.5	1
5	3	5.5	2
6	4.5	3	2
7	4.5	5.5	2
8	3	8	3
9	4.5	5.5	3
10	6	8	3
11	4.5	5.5	2
12	6	3	1
13	3	3	1
14	3	3	3
15	3	8	1
16	4.5	5.5	2
17	4.5	5.5	2
18	6	8	1

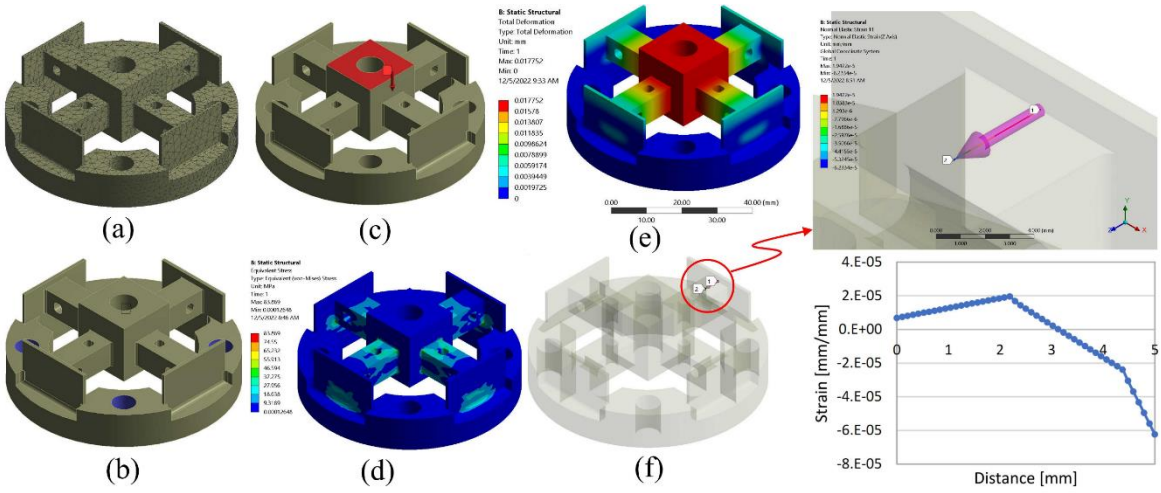

Fig. 2. Stages in FEM

Figure 2 shows FEM stages for obtaining stress, strain, and displacement of a force transducer structure. In order to accomplish the objective, certain assumptions were required. The force transducer was fixed in place in the bottom ring plate at its four-hole location. The load was applied such that it was uniformly distributed on top of the central hub of the structure. The target outputs of this analysis were to find out the sensitivity, cross-talk error, safety factor, and stiffness of the force transducer structure. The following equation was used to convert from strain to rated output voltage (mV/V) to obtain the sensitivities of the force transducer from numerical analysis [18]:

$$\frac{E_o}{E_i} = \frac{GF}{4}\varepsilon_{eq} = \frac{GF}{4}(\varepsilon_1 - \varepsilon_2 + \varepsilon_4 - \varepsilon_3) \tag{1}$$

where E_i is the fixed input voltage of the Wheatstone bridge of the strain sensor (5 V), E_o is the output voltage, GF is the gauge factor of the strain sensor, ε_1 and ε_4 are strain in tension surfaces, ε_2 and ε_3 are strain in compression surfaces.

2.4. FORCE TRANSDUCER OPTIMIZATION AND TEST RESULTS

The six characteristics of force transducer responses include the horizontal sensitivity (*Ss-H*), the vertical sensitivity (*Ss-V*), the cross-talk error (*Cs-E*), the safety factor (S_f), the horizontal stiffness (*k-H*) and the vertical stiffness (*k-V*). Table 3 summarizes the results of the measured and calculated response parameters. The variation range of *Ss-H*, *Ss-V*, *Cs-E*, S_f, *k-H* and *k-V* were respectively; 0.026–0.105 mV/N, 0.014–0.422 mV/N, 0.39–4.33 %, 0.76–3.38, 13.185–93.754 N/μm and 4.616–39.277 N/μm.

Table 3. Numerical analysis results, *Ss-H, Ss-V, Cs-E, Sf, k-H, k-V*

No. of Test Run	Geometry parameters			Response parameters					
	w (mm)	*l* (mm)	*t* (mm)	*Ss-H* (mV/N)	*Ss-V* (mV/N)	*Cs-E* (%)	S_f	*k-H* (N/μm)	*k-V* (N/μm)
1	4.5	5.5	2	0.046	0.108	0.85	3.53	56.13	21.94
2	3	8	1	0.075	0.058	0.39	1.72	31.26	19.59
3	4.5	5.5	2	0.045	0.107	0.82	3.59	56.09	21.94
4	3	3	1	0.064	0.014	4.03	1.85	36.49	28.17
5	4.5	8	2	0.049	0.198	1.06	3.10	41.63	13.97
6	4.5	5.5	1	0.081	0.074	0.95	1.65	30.65	18.05
7	6	5.5	2	0.060	0.243	2.20	3.14	37.64	12.25
8	4.5	5.5	2	0.046	0.108	0.84	3.57	56.11	21.95
9	3	5.5	2	0.038	0.054	1.05	3.67	64.56	29.65
10	6	8	1	0.105	0.334	2.65	1.30	13.19	4.62
11	6	8	3	0.048	0.422	2.24	1.53	23.47	5.41
12	6	3	1	0.058	0.057	1.85	1.75	30.18	16.85
13	6	3	3	0.037	0.114	1.11	4.58	69.83	24.27
14	4.5	5.5	3	0.036	0.124	0.96	4.34	72.07	24.62
15	3	8	3	0.030	0.110	1.54	4.60	75.66	25.96
16	3	3	3	0.026	0.037	1.66	5.77	93.75	39.28
17	4.5	5.5	2	0.046	0.108	0.83	3.55	56.12	21.97
18	4.5	3	2	0.038	0.049	2.05	3.74	63.87	28.94

Analysis of variance (ANOVA) was carried out to find the significant parameters and fitness of the quadratic regression model which affected the significant individual terms and their interaction on the selected responses. The ANOVA results of the horizontal sensitivity (*Ss*-*H*), the vertical sensitivity (*Ss*-*V*), the cross-talk error (*Cs*-*E*), the safety factor (S_f), the horizontal stiffness (*k*-*H*) and the vertical stiffness (*k*-*V*) have been shown in Tables 4–9 respectively.

Table 4. ANOVA result for horizontal sensitivity (*Ss*-*H*)

Source	Sum of Squares	df	Mean Square	F-value	p-value	Cont. %	Remarks
Model	0.0064	9	0.0007	24.77	< 0.0001		Significant
w–Through-hole Width	0.0005	1	0.0005	19.17	0.0024	8.72	Significant
l–Through-hole Length	0.0007	1	0.0007	24.70	0.0011	11.23	Significant
t–Thickness of Compliant Plate	0.0042	1	0.0042	147.12	< 0.0001	66.89	Significant
w x *l*	0.0002	1	0.0002	7.00	0.0294	3.18	Significant
w x *t*	4.50E-06	1	4.500E-06	0.1575	0.7018	0.07	Insignificant
l x *t*	0.0002	1	0.0002	7.72	0.0240	3.51	Significant
w^2	8.64E-06	1	8.641E-06	0.3025	0.5973	0.14	Insignificant
l^2	0.0000	1	0.0000	1.68	0.2305	0.77	Insignificant
t^2	0.0003	1	0.0003	12.08	0.0084	5.49	Significant
Error	1.000E-06	8	3.333E-07				
Total	0.0066	17				100	

Table 5. ANOVA result for vertical sensitivity (*Ss*-*V*)

Source	Sum of Squares	df	Mean Square	F-value	p-value	Cont. %	Remarks
Model	0.1947	9	0.0216	423.17	< 0.0001		Significant
w–Through-hole Width	0.0806	1	0.0806	1577.02	< 0.0001	41.74	Significant
l–Through-hole Length	0.0721	1	0.0721	1409.61	< 0.0001	37.34	Significant
t–Thickness of Compliant Plate	0.0073	1	0.0073	143.62	< 0.0001	3.78	Significant
w x *l*	0.0276	1	0.0276	539.99	< 0.0001	14.29	Significant
w x *t*	0.0006	1	0.0006	11.98	0.0086	0.31	Insignificant
l x *t*	0.0005	1	0.0005	9.40	0.0155	0.26	Insignificant
w^2	0.0035	1	0.0035	68.27	< 0.0001	1.81	Significant
l^2	0.0004	1	0.0004	6.88	0.0305	0.21	Insignificant
t^2	0.0005	1	0.0005	9.81	0.0140	0.26	Insignificant
Error	7.500E-07	8	2.500E-07				
Total	0.1952	17				100	

Table 6. ANOVA result for cross-talk error (*Cs*-*E*)

Source	Sum of Squares	df	Mean Square	F-value	p-value	Cont. %	Remarks
Model	11.21	9	1.25	4.71	0.02		Significant
w–Through-hole Width	0.1914	1	0.1914	0.7231	0.4198	2.101	Insignificant
l–Through-hole Length	0.7963	1	0.7963	3.01	0.121	8.743	Insignificant
t–Thickness of Compliant Plate	0.5595	1	0.5595	2.11	0.184	6.143	Insignificant
w x *l*	4.03	1	4.03	15.24	0.0045	44.247	Significant
w x *t*	0.0007	1	0.0007	0.0025	0.9614	0.008	Insignificant
l x *t*	1.85	1	1.85	6.99	0.0296	20.312	Significant
w^2	0.9297	1	0.9297	3.51	0.0978	10.208	Insignificant
l^2	0.7309	1	0.7309	2.76	0.1351	8.025	Insignificant
t^2	0.0195	1	0.0195	0.0735	0.7931	0.214	Insignificant
Error	2.1205	8	0.4235				
Total	13.33	17				100	

Table 7. ANOVA result for safety factor (*Sf*)

Source	Sum of Squares	*df*	Mean Square	*F*-value	*p*-value	Cont. %	Remarks
Model	27.07	9	3.01	37.47	< 0.0001		Significant
w–Through-hole Width	2.82	1	2.82	35.13	0.0004	10.748	Significant
l–Through-hole Length	2.96	1	2.96	36.87	0.0003	11.282	Significant
t–Thickness of Compliant Plate	15.75	1	15.75	196.21	< 0.0001	60.030	Significant
w x *l*	0.605	1	0.605	7.54	0.0252	2.306	Significant
w x *t*	1.75	1	1.75	21.78	0.0016	6.670	Significant
l x *t*	1.66	1	1.66	20.63	0.0019	6.327	Significant
w^2	0.0189	1	0.0189	0.2358	0.6403	0.072	Insignificant
l^2	0.0127	1	0.0127	0.1587	0.7008	0.048	Insignificant
t^2	0.6601	1	0.6601	8.22	0.0209	2.516	Significant
Error	0.6422	8	0.1287				
Total	27.71	17				100	

Table 8. ANOVA result for horizontal stiffness (*k*-*H*)

Source	Sum of Squares	*df*	Mean Square	*F*-value	*p*-value	Cont. %	Remarks
Model	7540.23	9	837.8	146.61	< 0.0001		Significant
w–Through-hole Width	1623.28	1	1623.28	284.07	< 0.0001	22.030	Significant
l–Through-hole Length	1186.51	1	1186.51	207.64	< 0.0001	16.103	Significant
t–Thickness of Compliant Plate	3725.68	1	3725.68	651.99	< 0.0001	50.563	Significant
w x *l*	200.31	1	200.31	35.05	0.0004	2.719	Significant
w x *t*	334.7	1	334.7	58.57	< 0.0001	4.542	Significant
l x *t*	222.9	1	222.9	39.01	0.0002	3.025	Significant
w^2	34.84	1	34.84	6.1	0.0388	0.473	Significant
l^2	10.17	1	10.17	1.78	0.2189	0.138	Insignificant
t^2	30	1	30	5.25	0.0512	0.407	Insignificant
Error	45.71	8	9.1402				
Total	7585.95	17				100	

Table 9. ANOVA result for vertical stiffness (*k*-*V*)

Source	Sum of Squares	*df*	Mean Square	*F*-value	*p*-value	Cont. %	Remarks
Model	1237.17	9	137.46	332.47	< 0.0001		Significant
w–Through-hole Width	628.07	1	628.07	1519.04	< 0.0001	50.924	Significant
l–Through-hole Length	461.76	1	461.76	1116.8	< 0.0001	37.440	Significant
t–Thickness of Compliant Plate	104.04	1	104.04	251.62	< 0.0001	8.436	Significant
w x *l*	10.58	1	10.58	25.6	0.001	0.858	Significant
w x *t*	10.73	1	10.73	25.94	0.0009	0.870	Significant
l x *t*	16.18	1	16.18	39.13	0.0002	1.312	Significant
w^2	1.49	1	1.49	3.6	0.0945	0.121	Insignificant
l^2	0.1553	1	0.1553	0.3757	0.5569	0.013	Insignificant
t^2	0.3396	1	0.3396	0.8214	0.3913	0.028	Insignificant
Error	3.31	8	0.6616				
Total	1240.48	17				100	

Table 4 shows ANOVA results of the horizontal sensitivity (*Ss*-*H*). The quadratic regression model had an *F*-value of 24.77 and a *p*-value of less than 0.0001, which implied that the model was significant at the 95% confidence level. The p-value represents the probability of error and is used to check the significance of each regression coefficient. It is also indicative of the interaction effect of each cross parameter. Hence, p-values of less than 0.0500 indicated that the model terms were significant. In this case A, B, C, AB, BC, C^2 were

significant model terms. Values greater than 0.1000 indicated that the model terms were not significant. It was found that the thickness of compliant plate (t) had the most influence on (*Ss-H*) with 67.09% of contribution, followed by the through hole length (l) and through holes width (w) with 10.99% and 8.72 % of contribution respectively. The interaction terms (t^2), (*l* x *t*) and (*w* x *l*) were also found to be significant with small contributions of (5.43, 3.59 and 3.37)%, respectively.

The ANOVA results of the vertical sensitivity (*Ss-V*) have been presented in Table 5, indicating that the significant parameters were (*w*) and (*l*) with the respective contributions of 41.74% and 37.34%, followed by (*w* x *l*) and (*t*) with (14.29 and 3.78)% of contributions, respectively. The other terms were found to be insignificant with small contributions (less than 2 %).

Table 6 describes the ANOVA of cross-talk error (*Cs-E*). It can be seen that only two terms were found to be significant, (*w* x *l*) and (*l* x *t*) with the respective contributions of 44.25% and 20.31%. The other terms were found not to be significant with *p*-values greater than 0.0500.

The ANOVA results of the safety factor (S_f) have been shown in Table 7. It was noted that the thickness of compliant plate (*t*) was the factor most influencing (S_f) with a contribution of 60.03%, followed by the through hole length (*l*) and the through hole width (*w*) with the contributions of 11.28% and 10.75% respectively. The other terms gave small contributions while the terms (w^2) and (l^2) were not significant.

The ANOVA results of the horizontal stiffness (*k-H*) have been shown in Table 8. It was clear that (*t*), (*w*) and (*l*) had more influence on (*k-H*) with the respective contributions of 50.56%, 22.03% and 16.1%. All interactions terms gave small contribution of under 5%, but (l^2) and (t^2) were not significant.

The ANOVA results of the vertical stiffness (*k-V*) have been tabulated in Table 9. It could be clearly observed that all terms were significant except the quadratic term which showed a *p*-value greater than 0.0500. The term gave more influence on (*k-V*) is (*w*) with the contribution 50.92%, and followed by (*l*) and (*t*) with the contribution 37.44% and 8.44% respectively.

The relationships between the dependent variables or responses (*Ss-H*, *Ss-V*, *Cs-E*, S_f, *k-H* and *k-V*) and the independent variables or factors (*w*, *l* and *t*) are expressed by the following equation:

The horizontal sensitivity (*Ss-H*) model is given below in Eq. (2). Its coefficient of determination (R^2) is 96.54%.

$$Ss-H = 0.102 - 0.011w + 0.09l - 0.056t + 0.001wl + 0.0005wt - 0.002lt + 0.00079w^2 - 0.00067l^2 + 0.01128t^2 \tag{2}$$

The vertical sensitivity (*Ss-V*) model is given by the following Eq. (3). Its coefficient of determination (R^2) is 99.7%.

$$Ss-V = 0.397 - 0.182w - 0.063l + 0.038t + 0.016wl + 0.006wt + 0.003lt + 0.016w^2 + 0.0018l^2 - 0.0136t^2 \tag{3}$$

The cross-talk error (*Cs-E*) model is given by the following Eq. (4). Its coefficient of determination (R^2) is 84.12%.

$$Cs-E=15.919-3.304w-2.264l-0.982t+0.189wl+0.006wt+0.192lt$$
$$+0.26w^2+0.083l^2-0.085t^2 \tag{4}$$

The safety factor (S_f) model is given by the following Eq. (5). Its coefficient of determination (R^2) is 97.68%.

$$Sf=-5.876+1.007w+0.597l+5.633t-0.073wl-0.312wt-0.182lt$$
$$-0.037w^2-0.011l^2-0.494t^2 \tag{5}$$

The horizontal stiffness (*k-H*) model is given by the following Eq. (6). Its coefficient of determination (R^2) is 99.4%.

$$k-H=-71.037+21.813w+9.28l+63.629t-1.334wl-4.312wt-2.111lt$$
$$-1.594w^2-0.31l^2-3.327t^2 \tag{6}$$

The vertical stiffness (*k-V*) model is given by the following Eq. (7). Its coefficient of determination (R^2) is 99.73%

$$k-V=24.055+0.91w+0.221l+11.244t-0.307wl-0.772wt-0.569lt$$
$$-0.329w^2-0.038l^2-0.354t^2 \tag{7}$$

Figure 3 shows a comparison of the responses that were fit to the quadratic model with those that were simulated. It can be seen from these results that the deviations between the predicted values and the simulation ones were not very significant.

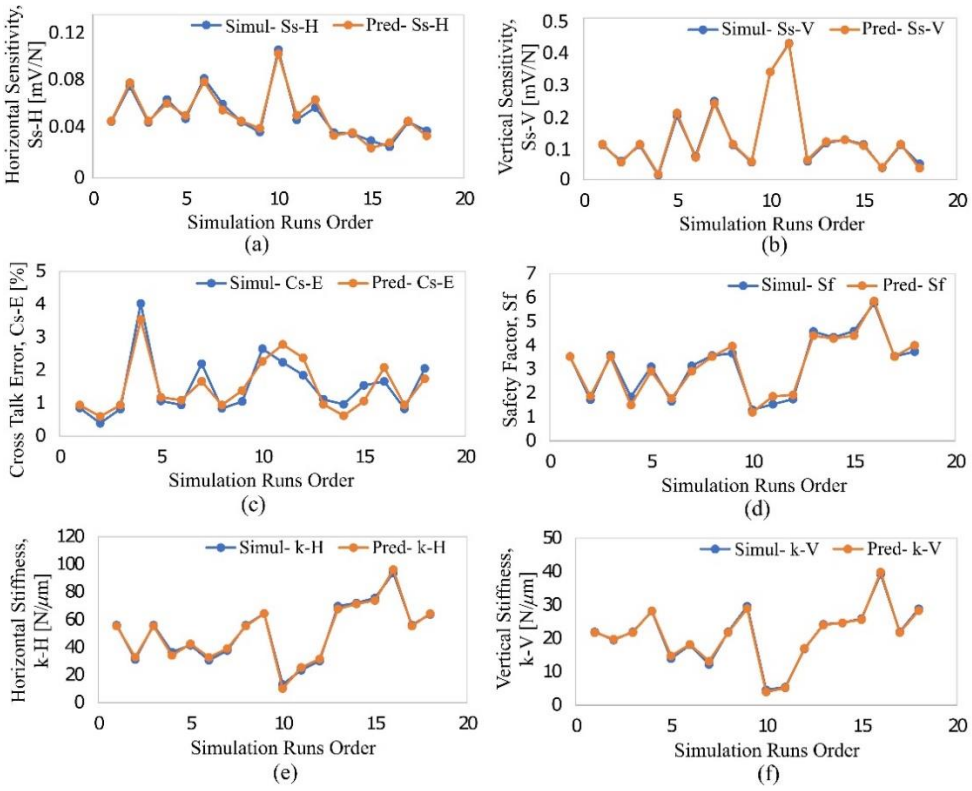

Fig. 3. Comparison between measured and predicted values of response parameters

The variation values of the horizontal sensitivity (*Ss-H*) have been displayed in Fig. 4a, which is a 3D response surface diagram, in accordance with the through-hole width (*w*) and length (*l*). It can be seen that an increase in value for (w) results in a significantly increased value for (*Ss-H*). But on the other hand, according to Fig. 4b, the value of *Ss-H* rose when (*t*) got smaller and when (*w*) got larger.

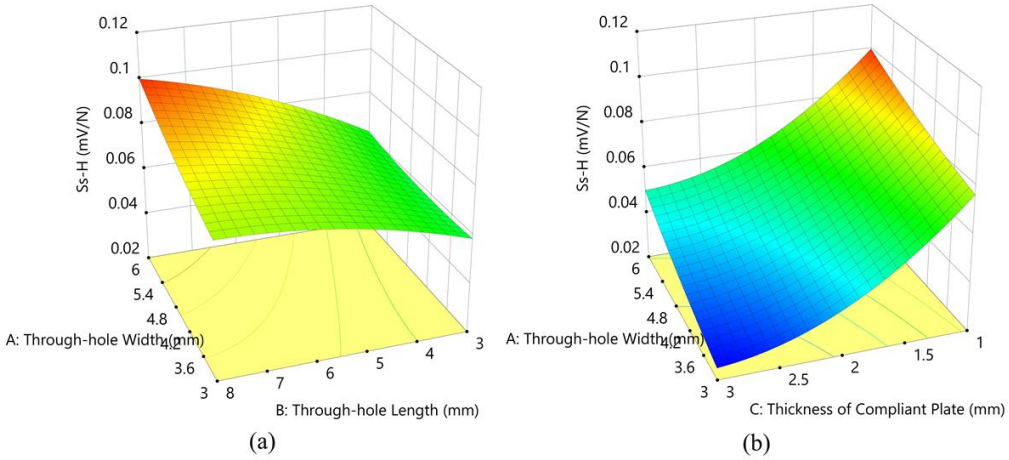

Fig. 4. Comparison Response surface of *Ss-H*. (a) as function of (*w*) and (*l*); (b) as function of (*w*) and (*t*)

Figure 5a shows the interaction of through-hole width (*w*) and through-hole length (*l*) with respect to vertical sensitivity (*Ss-V*). It is clear to see that the greatest value of (*Ss-V*) may be attained when the (*w*) is increased from 3 mm to 6 mm and (*l*) is increased from 3 mm to 8 mm. In a similar manner, the response that was dependent on (*w*) and (*t*) got higher, which led to the maximum vertical sensitivity (*Ss-V*) as seen in Fig. 5b.

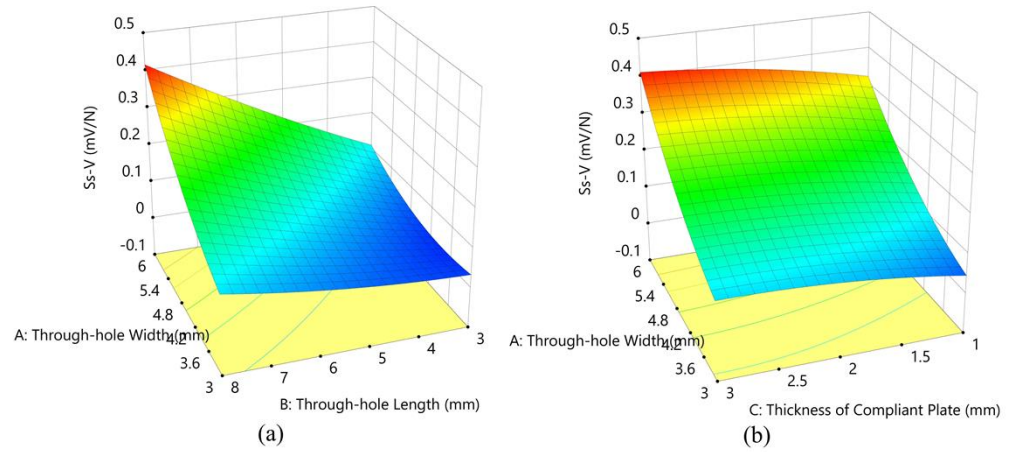

Fig. 5. Response surface of *Ss-V*. (a) as function of (*w*) and (*l*); (b) as function of (*w*) and (*t*)

Cross-talk error (*Cs-E*) interaction between (*w*) and (*l*) has been shown in Fig. 6a. It is evident that the lowest (*Cs-E*) value can be reached by decreasing (*w*) from 6 mm to

3 mm and increasing (*l*) from 3 mm to 8 mm. On the other hand, as seen in Fig. 6b, the value of (*Cs-E*) decreases as (*w*) and (*t*) increase.

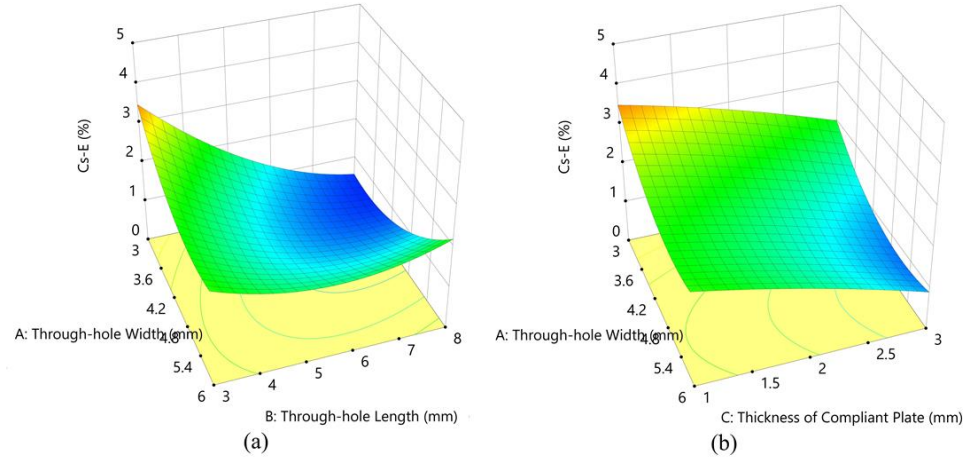

Fig. 6. Response *E*. (a) as function of (*w*) and (*l*); (b) as function of (*w*) and (*t*)

Figure 7 illustrates the changes of the safety factor (S_f) as a function of (*w*) and (*l*). According to the 3D graph, an increase in (*w*) significantly increases the safety factor when the thickness of a compliant plate (*t*) is increased. It is reasonable that the strength of structure increased with the increasing of the (*t*). The significance of the result is that the (*t*) is highly related to safety factor.

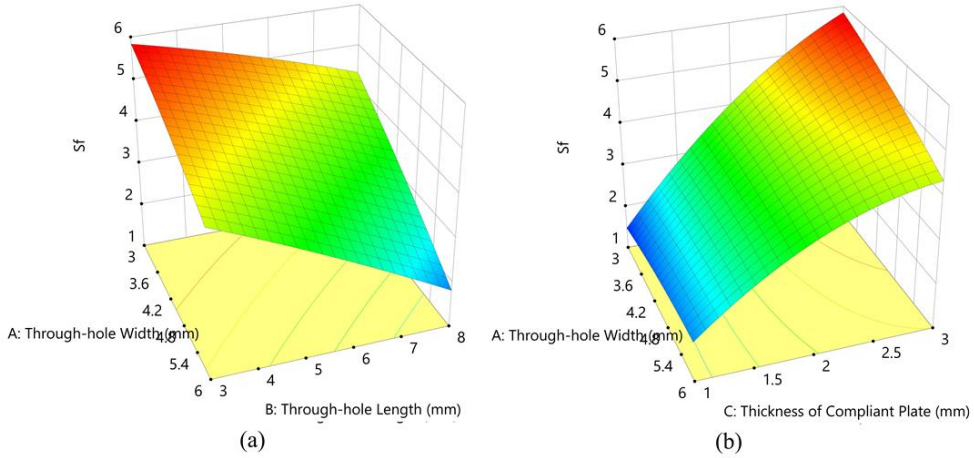

Fig. 7. Response surface of S_f. (a) as function of (*w*) and (*l*); (b) as function of (*w*) and (*t*)

Figure 8 shows the variations of the horizontal stiffness (*k-H*) as a function of through-hole width (*w*) and through-hole length (*l*). It is obvious that the largest value of (*k-H*) was obtained when the (*w*) dropped from 6 mm to 3 mm and likewise (*l*) was decreased from 8 mm to 3 mm. The relevance of the result to the (*t*) is significant in relation to the horizontal stiffness.

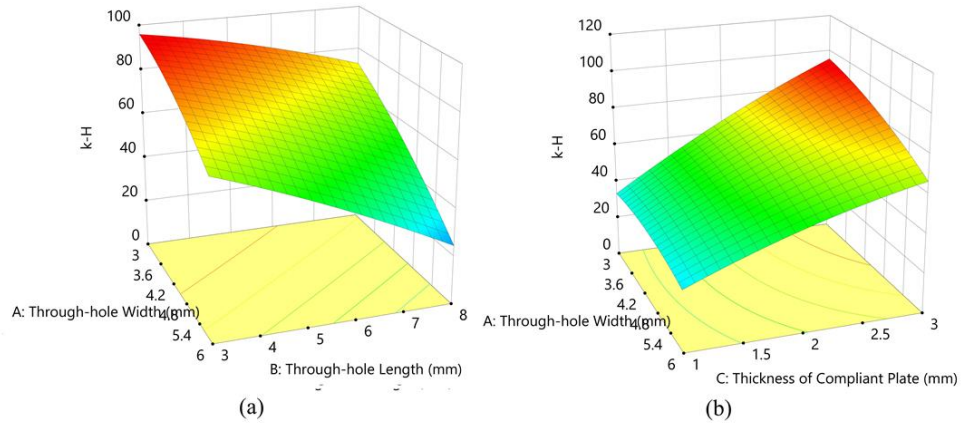

Fig. 8. Response surface of *k-H*. (a) as function of (*w*) and (*l*); (b) as function of (*w*) and (*t*)

Figure 9 shows the varying values of vertical stiffness (*k-V*) in a 3D response surface diagram. It is clear that a decrease in the values of (*w*) and (*l*) leads to a large increase in the value of (*k-V*). On the other hand, as shown in Figure 9b, the value of *k-V* increases as (*t*) increases. Consequently, the (*t*) is also highly relevant with regards to the vertical stiffness.

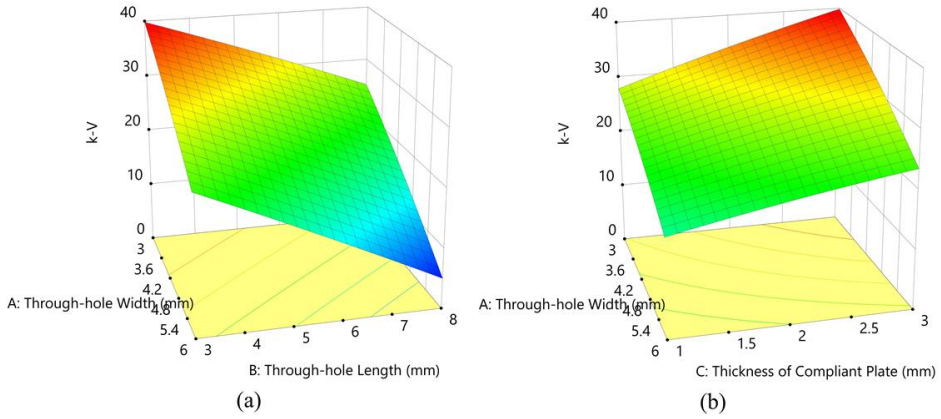

Fig. 9. Response surface of *k-V*. (a) as function of (*w*) and (*l*); (b) as function of (*w*) and (*t*)

2.5. OPTIMIZATION OF FORCE TRANSDUCER GEOMETRY

For the optimization study of the force transducer structure, the objective was to simultaneously optimize the levels of the independent variables in order to achieve optimal sensitivity, rigidity and cross-talk error. Utilizing a desirability function is an effective method for optimizing multiple responses simultaneously. To optimize the use of an overall desirability function, it was necessary to formulate the specifications for each of the factors and responses listed in Table 10. The horizontal and vertical sensitivities were specified to be maximum with the range 0.025–0.075 mV/N with a high importance index of 5. The cross-talk error was to be minimized with a range of 1% to 3% and an importance index of 3, but

the safety factor and the stiffness have to be maximized between the ranges of 1.2 to 3 and 15 to 50 N/m with an importance index of 2, respectively.

Table 10. Specification, goal and parameter ranges for optimization.

Name	Goal	Lower Limit	Upper Limit	Lower Weight	Upper Weight	Importance	Desirability
A:Through-hole Width	is in range	3	6	1	1	3	1
B:Through-hole Length	is in range	3	8	1	1	3	1
C:Thickness of Compliant Plate	is in range	1	3	1	1	3	1
Ss-H	maximize	0.025	0.075	0.1	1	5	0.95
Ss-V	maximize	0.025	0.075	0.1	1	5	0.97
Cs-E	minimize	1	3	1	0.1	3	1
S_f	maximize	1.2	3	1	1	2	1
k-H	maximize	15	50	1	1	2	0.99
k-V	maximize	15	25	1	1	2	0.82

Table 11 presents the optimal parameters of force transducer structure, where dimensions of the through-hole width (*w*), length (*l*) and the compliant plate thickness (*t*) were 3.41, 6.19 and 1.55 mm respectively with the highest desirability of 0.97. The values obtained for overall and individual desirability were close to the optimal value of 1. This demonstrated that the dimensions of the force transducer structure had been optimally designed.

Table 11. Optimal geometry parameters for force transducer structures

Number	*w*	*l*	*t*	*Ss-H*	*Ss-V*	*Cs-E*	S_f	*k-H*	*k-V*	Desirability	
1	**3.41**	**6.19**	**1.55**	**0.055**	**0.063**	**1.000**	**3.000**	**49.735**	**23.797**	**0.970**	**Selected**
2	3.36	6.30	1.55	0.055	0.063	0.986	3.000	49.652	23.773	0.969	
3	3.98	5.49	1.57	0.055	0.070	1.050	3.000	49.553	22.883	0.967	
4	3.70	5.53	1.55	0.055	0.060	1.113	3.000	50.134	23.961	0.966	
5	4.19	5.39	1.59	0.055	0.077	1.049	3.000	49.115	22.203	0.964	

3. DESIGN AND FABRICATION OF THE THREE-AXIS STATIONARY DYNAMOMETER

The dynamometer which had been designed and developed was a stationary dynamometer capable of measuring three components of cutting force for milling processes and other technical applications. The utilized force sensor element type had been optimized using the response surface method. In contrast to the design and shape of the previously reported dynamometer, which used sensor elements in the form of four octagonal rings [25–27], leaf-type flexure elements [22] and utilized a center quadrangular prism surrounded by four force-sensing elastic elements [30], the primary force sensor of this dynamometer was a modified Maltese cross-beam.

Figure 10 depicts the proposed schematic design of the stationary dynamometer system. The main components of the dynamometer include a base plate, four optimized cross-beam force transducer, a top plate and side covers. The cutting force that occurs during the milling

process will be continued by the workpiece, which is located on the top plate and is clamped with a bolt on each transducer. Thus, the cutting force acting on the top plate will deform the elastic component of the transducer structure in the form of cross beams, which contain horizontal and vertical parallel flat plates. So, the strain due to deformation that occurs on the surface of the transducer structure can be detected by a piezo-resistive strain sensor whose orientation follows the three-dimensional coordinate axes of forces namely F_x, F_y and F_z.

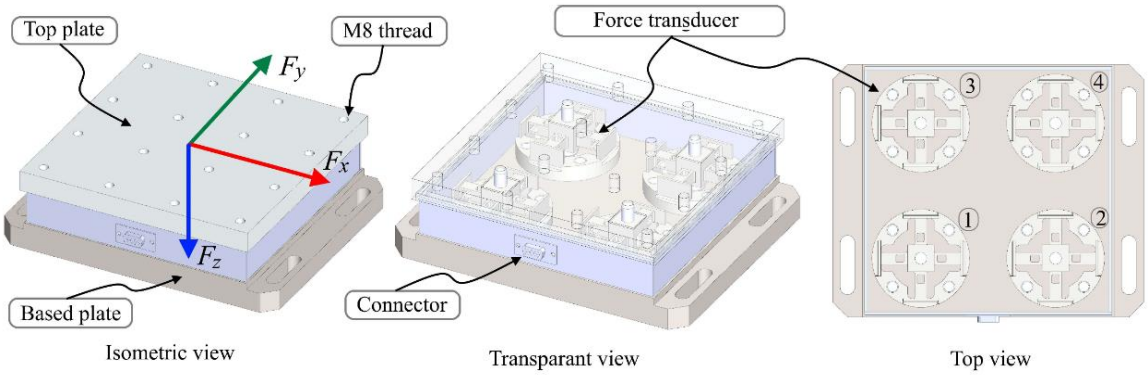

Fig. 10. Schematic design of a stationary dynamometer using four modified Maltese cross-beam force transducers

3.1. PIEZORESISTIVE STRAIN SENSOR ARRANGEMENT IN FORCE TRANSDUCER

When the piezoresistive strain sensor is attached on the surface flexural structure or sensing element, the resistance of the strain sensor will show variation upon application of the external force. The strain could be converted into a voltage signal by a Wheatstone bridge circuit. Figure 11 depicts the proven correct location of the strain sensor which has been described in the FEM result section above. In this works, the strain sensor arrangement on a single force transducer is very important before being assembled for the main table dynamometer elements.

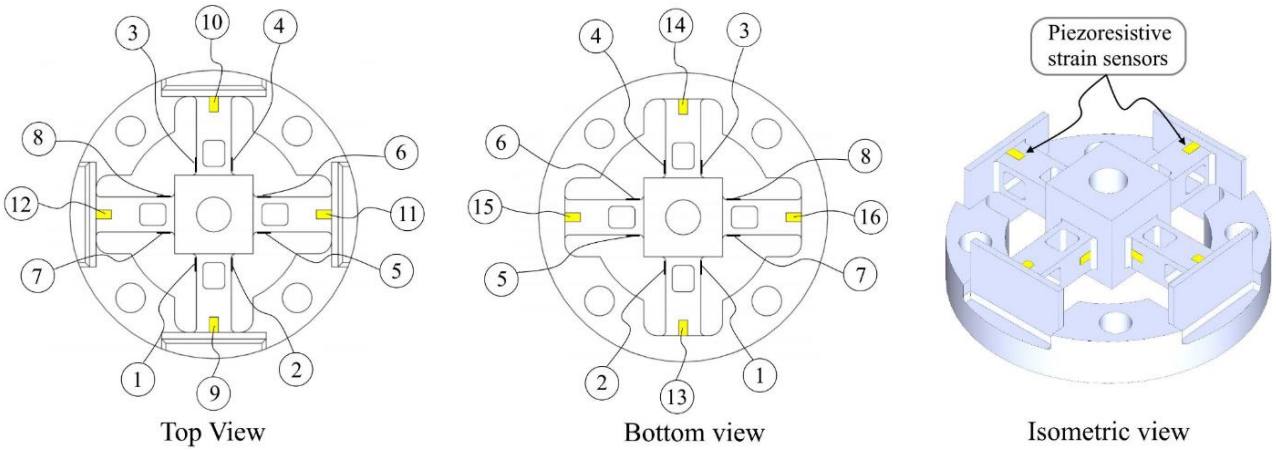

Fig. 11. Piezoresistive strain sensor locations in a single force transducer

In order to detect the presence of an external force acting on a single force transducer, full Wheatstone bridges were utilized as shown in Fig. 12. The arrangement of piezo-resistive strain sensors for detecting the force in *x*-axis direction (F_x) has been described in Fig. 12a. The strain sensors S-01 and S-03 were subjected to compressive stress while S-02 and S-04 were subjected to tensile stress, respectively. The force in *y*-axis direction (F_y) was detected by S-05 and S-07 in which these sensors were subjected to compressive stress as shown in Fig. 12b, whereas S-06 and S-08 were subjected to tensile stress. The vertical force in *z*-axis direction (F_z) was affected by four beams with the strain sensor arrangement as shown in Fig. 12c. Sensors S-09, S-10, S-11 and S-12 were subjected to compressive stress, while sensors S-13, S-14, S-15 and S-16 were subjected to tensile stress.

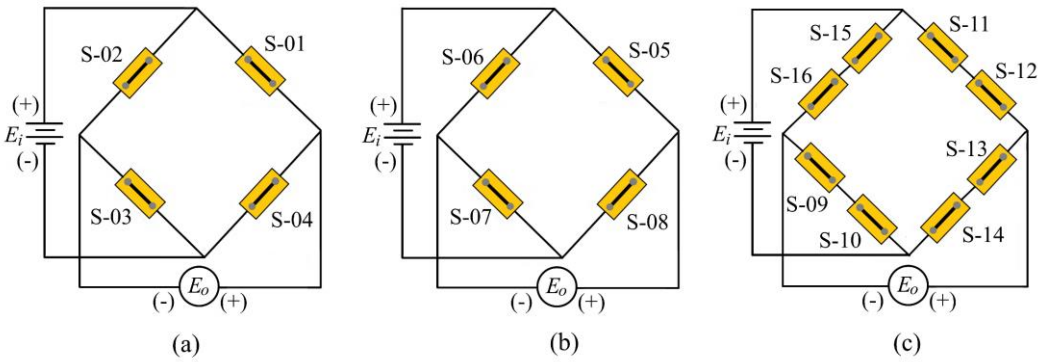

Fig. 12. Wheatstone bridges circuit for detection of forces in a single force transducer: (a) *Fx*; (b) *Fy*; and (c) *Fz*

All strain sensors used in this work were linear strain sensor SSC-350-B-F5 (UTOP) with the nominal resistance of 350 Ω. The gauge factor (*GF*) of this sensor was 150, the length of the gauge was 6 mm, and the width of the gage was 3.5 mm. The actual strain could be obtained by the following equation [18]:

$$\frac{\Delta L}{L} = \varepsilon = \frac{\Delta R/R}{GF} \tag{8}$$

where ε is the strain detected by the strain sensor, R is the initial resistance of sensor, ΔR is the differential resistance, L is the original length, and ΔL is gauge elongation due to stress.

3.2. CONFIGURATION THE FORCE TRANSDUCER IN THE STATIONARY DYNAMOMETER

A stationary dynamometer was developed with the use of four separate force detecting elements that had been optimized earlier. Figure 10 illustrates how the four different components of the base plate dynamometer were arranged in the unit. Figure 13 demonstrates the configuration of the wiring dynamometer system, which made use of four different force sensing devices. Each force sensor and each channel had an output terminal, which included two pins of output for detecting tension stress and two pins for detecting compression stress.

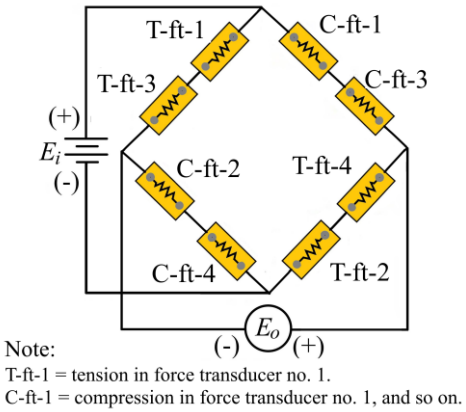

Fig. 13. Wheatstone bridges circuit for detection each channel of force in the dynamometer unit

3.3. CONSTRUCTION OF THE DYNAMOMETER AND DATA ACQUISITION SYSTEM

The structure of the developed stationary dynamometer consisted of the top and bottom plates, force transducer with a piezoresistive strain sensor on them and the electrical connections required to create Wheatstone bridge circuits. Using a CNC machining process, the stationary dynamometer's structure, which includes four force transducers, was manufactured. For the force transducer and top plate structures, the aluminum alloy 5083-H112 was chosen, while the base plate was made of stainless steel 304. The force transducer's final dimensions, which are 5 mm, 6 mm, and 1.5 mm in *w*, *l*, and *t*, respectively, are based on the optimization's closest size dimensions. To ensure that the dynamometer was waterproof, all of its edges were covered with aluminum plates and sealed with silicone rubber. Fig. 14 shows the photograph of the fabricated stationary dynamometer. Through the connector on the dynamometer unit, three channels of cutting force signals were transmitted via multi-conductor cable to the data acquisition system of the NI-9237 which has a 24-bit A/D converter and the maximum sampling rate of 50 kHz. Then signals were converted from analogy data to digital data before recording and displaying it using Signal-Express software.

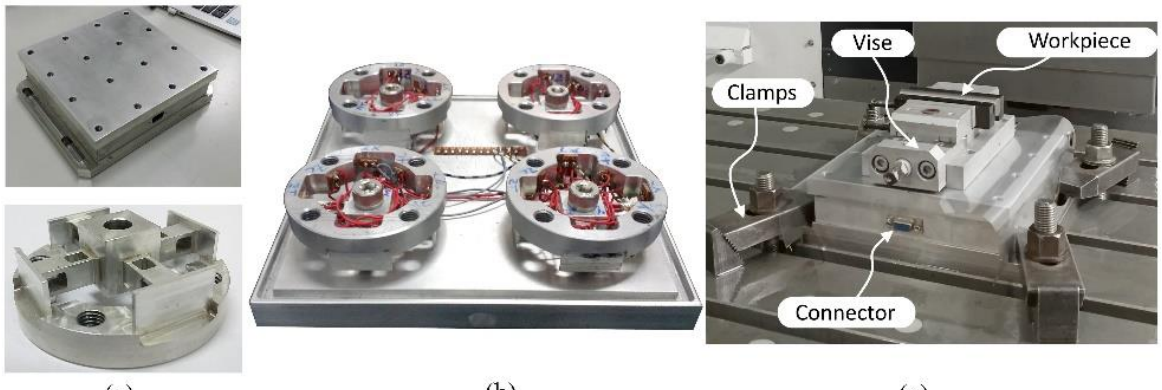

Fig. 14. Photograph of the prototype: (a) primary component units; (b) force transducer with sensors installed; and (c) finished prototype on the CNC table

4. TESTING OF A DEVELOPED STATIONARY DYNAMOMETER

4.1. CHARACTERIZATION OF STATIONARY DYNAMOMETER

A static calibration can be used to determine the relationship between a constant quantity of loads and the output signals for each channel of the dynamometer. Using a hydraulic press equipped with a standard load cell (Zemic-H3-C3), static calibration was performed to evaluate the performance of the dynamometer following its design and completed construction. Three orientations (x, y and z) were subjected to increasing loads ranging from 0 to 2000 N in increments of 50 N. Figure 15 shows the static calibration test setup of the dynamometer.

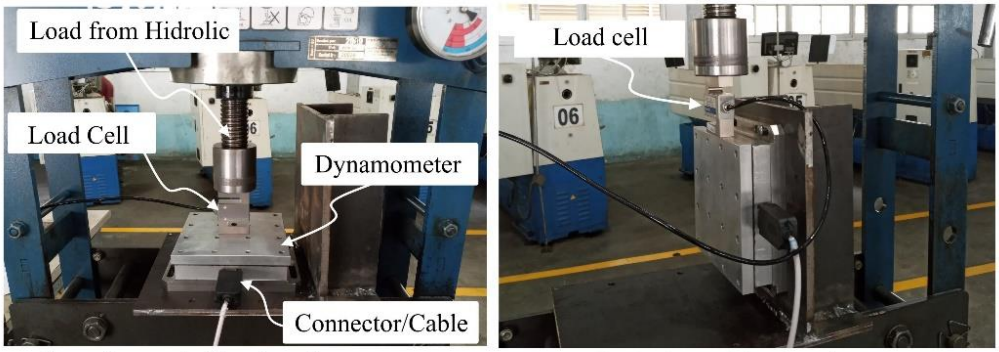

Fig. 15. Dynamometer setup in static calibration test

As a result, calibration graphs were created to relate the averaged output values to the quantities of the cutting forces. In addition to recording readings for the associated channel, readings from the other channels were also captured. Consequently, the impact of each loading on directions other than its own was studied. The calibration graphs for forces along the x-direction (F_x), y-direction (F_y) and z-direction (F_z), as well as their interactions, have been shown in Fig. 16.

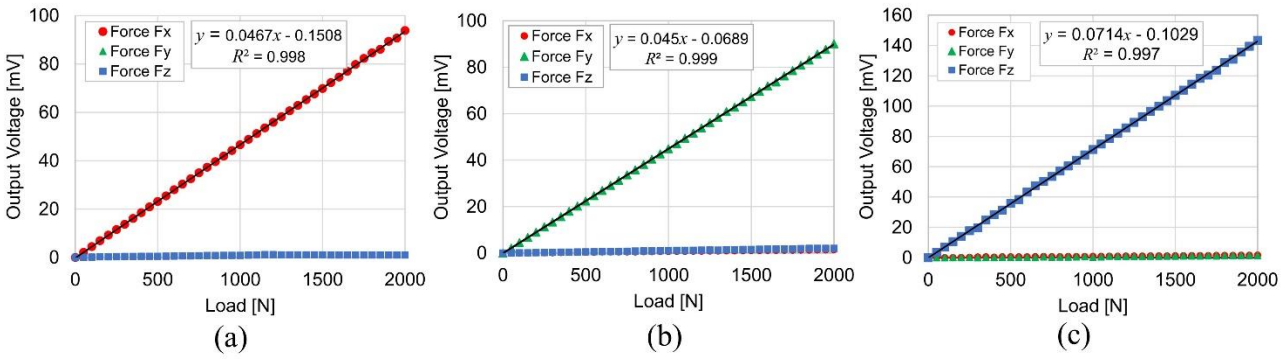

Fig. 16. Dynamometer calibration curve: (a) F_x direction; (b) F_y direction; (c) F_z direction

To ensure that the results were consistent, the measurements were performed five times and the average values were plotted on a graph. Because the force transducer can be considered as a linear system, the following relationship can be described:

$$S = [C]F \tag{9}$$

$$\begin{bmatrix} S_{F_x} \\ S_{F_y} \\ S_{F_z} \end{bmatrix} = \begin{bmatrix} C_{11} & C_{12} & C_{13} \\ C_{21} & C_{22} & C_{23} \\ C_{31} & C_{32} & C_{33} \end{bmatrix} \begin{bmatrix} F_x \\ F_y \\ F_z \end{bmatrix} \tag{10}$$

where F is the vector of the input component force value [F_x F_y F_z], C is an element of matrix or calibration matrix, and S is the vector of voltage output value. According to the experimental results, the static calibration matrix can be obtained as follows:

$$\begin{bmatrix} 46.363 & -0.843 & 0.859 \\ 0.731 & 44.789 & 1.034 \\ 0.812 & 0.552 & 71.192 \end{bmatrix}$$

The calibration curve and matrix made it abundantly clear that the sensitivities of the stationary dynamometer were obtained at about 46.363 μV/N, 44.789 μV/N and 71.192 μV/N. The cross-talk error for the F_x, F_y, and F_z directions have all been shown in Table 12. The F_y component had a maximum error of around 1.88% in the F_y direction, although the error for the other components did not exceed 1.75% in any direction. This is indicative of low coupling and a successful design with minimal cross-sensitivity levels. While cross-sensitivity is a complex phenomenon, it is nearly impossible to obtain precise findings for it because of the many external elements involved [18, 27].

Table 12. Cross-talk error of the dynamometer based on static calibration test

Force Direction	Cross-talk error (%)		
	F_x	F_y	F_z
F_x	-	1.88	1.21
F_y	1.57	-	1.45
F_z	1.75	0.77	-

The linearity, hysteresis and repeatability of the developed stationary dynamometer were investigated for each of the three directions of forces in order to further assess its static characteristics. Fig. 16 demonstrate the change in output to force conversion for each component, which may serve as a useful indication of linearity in the output reading of the bridge. Each component was loaded with 500 N, 1000 N and 1500 N to further evaluate the instrument's linearity and assess its ability to measure loads outside of the calibration range. The hysteresis test verified the difference between reading the increasing load and reading the decreasing load on the dynamometer by gradually increasing the loading from 0 to 2000 N and vice versa for each component. Furthermore, the repeatability of the dynamometer was

evaluated to confirm its consistency. This was performed by repeatedly loading each component with 10, 50 and 100 N five times, resulting in a total of 15 measurements for each component. The average and the standard deviation were the two parameters chosen to more effectively present the repeatability error. Table 13 shows linearity, hysteresis and repeatability errors of each component for the applied forces. It is evident that the greatest errors of the dynamometer did not exceed 1%.

Table 13. Linearity, hysteresis and repeatability errors for each axis of the dynamometer.

Force Direction	Average of linearity error (%)	Hysteresis error (%)	Repeatability error (%)		
			10 N	50 N	100 N
F_x	0.21	0.26	0.08	0.46	1.58
F_y	0.14	0.19	0.35	0.63	1.74
F_z	0.06	0.98	0.12	0.82	1.95

When using a stationary dynamometer for the machining process, the cutting force fluctuates, so the system's reaction to dynamic excitation is important to take into consideration. The identification of the main structure of the developed stationary dynamo-meter was accomplished in terms of a modal test. The dynamometer was fixed on the machine tool table of a CNC milling machine and excited in three directions (*x*, *y*, and *z*-axis) using a Piezotronics impulse force hammer (086C03). A piezotronics accelerometer (352C33) was attached to the dynamometer component to collect a dynamic response signal from the dynamometer structure. The excitation test in each direction was run three times to reduce errors. The signals were acquired by a data acquisition device (NI-9250) and by using LabVIEW software with a sampling rate of 50 kHz. Natural frequency graphs are displayed in Fig. 17, which was generated by the modal analysis.

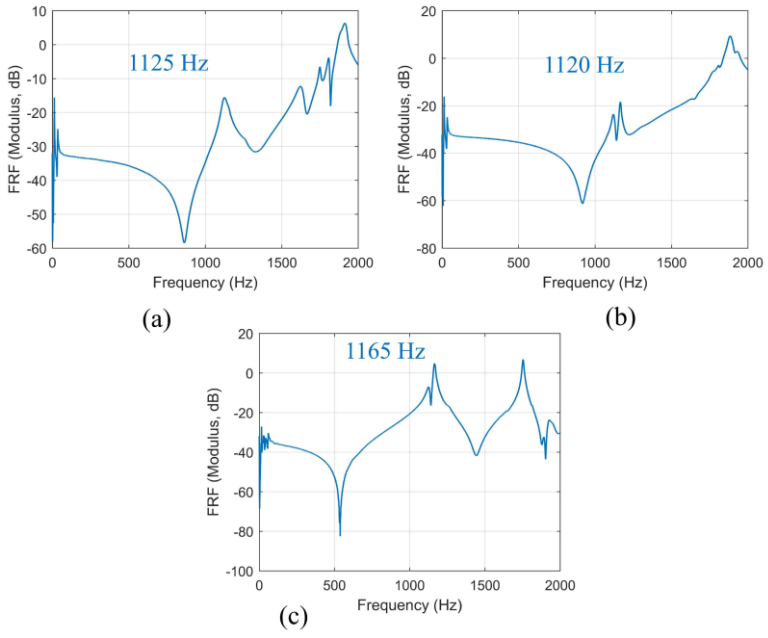

Fig. 17. Natural frequency of dynamometer: (a) *x*-direction; (b) *y*-direction; (c) *z*-direction

The observed natural frequencies of the stationary dynamometer structure were 1125 Hz, 1120 Hz, and 1165 Hz, respectively, when measured along the axes *x*, *y*, and *z*, respectively. These findings showed that the dynamometer structure as it was developed was suitable for both conventional milling and high-speed machining.

A thermal test was also conducted to assess the temperature effects on the dynamometer's reading cutting force. Using a heater plate, the top plate of the dynamometer was warmed from 30ºC to 40ºC. Two thermocouples have been attached to measure the external temperature on the top and bottom plates of the dynamometer. Figure 18 shows the static force offset generated by the thermal expansion effect of the cross-beam beam force transducer when the temperature was increased. It can be seen that the effect of the temperature rise on the surface of the dynamometer top plate will affect the dynamometer's reading. The channel that has the greatest influence due to thermal expansion is the *y*-channel, showing a signal change of 1.6 N/ºC. while the *x* and *z* channels are respectively 0.45 and 0.6 N/ºC. This indicates that changes in temperature within the range of 10°C in the structure will affect the uncertainty in the dynamometer readings of around 4.5 to 16 N.

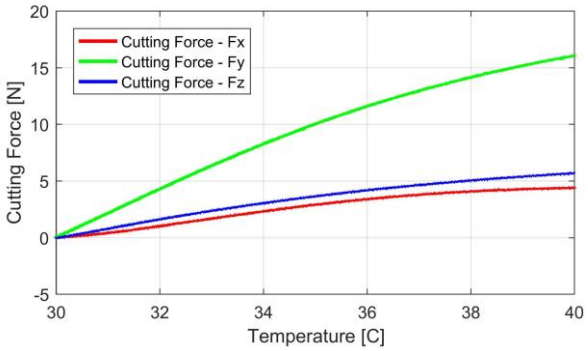

Fig. 18. The effect of temperature on the cutting force reading

4.2. VALIDATION TEST OF THE DYNAMOMETER IN MILLING PROCESS

Testing the developed stationary dynamometer in actual machining operations is an important procedure for assessing the accuracy and precision of the cutting force measurements. Under dry conditions, the test was conducted with slot cutting on a milling machine (Knuth UFM2). The tests were conducted on 15×90×100 mm polymer composite plates using a 2-flute HSS end-mill with an 8 mm diameter as the cutting tool. The machining parameters for the experiments were fixed at an axial depth of cut of 0.5 mm. The spindle speed was kept at 1200 rpm, and the feed rate was kept at 0.25 mm/tooth. Figure 19 shows the actual machining test setup. A comparison was made between the data acquired from the newly developed dynamometer and the data obtained from the reference dynamometer (Kistler 9129AA).

The most stable sections of the milling operation were utilized to collect data on the cutting forces that were acting along each axis. Readings of the steady cutting force obtained from both the developed dynamometer and the reference dynamometer are depicted in

Fig. 20. Both signals have been superimposed, as can be seen, to demonstrate that the cutting force peaks produced by each tooth of the cutting tool were clearly captured by both dynamometers.

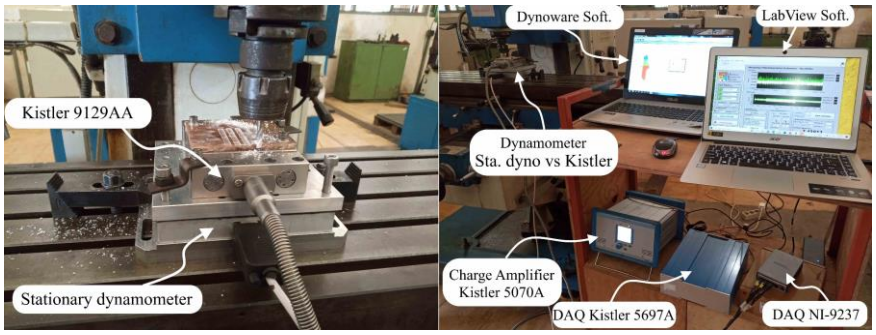

Fig. 19. Machining setup for validation of developed dynamometer

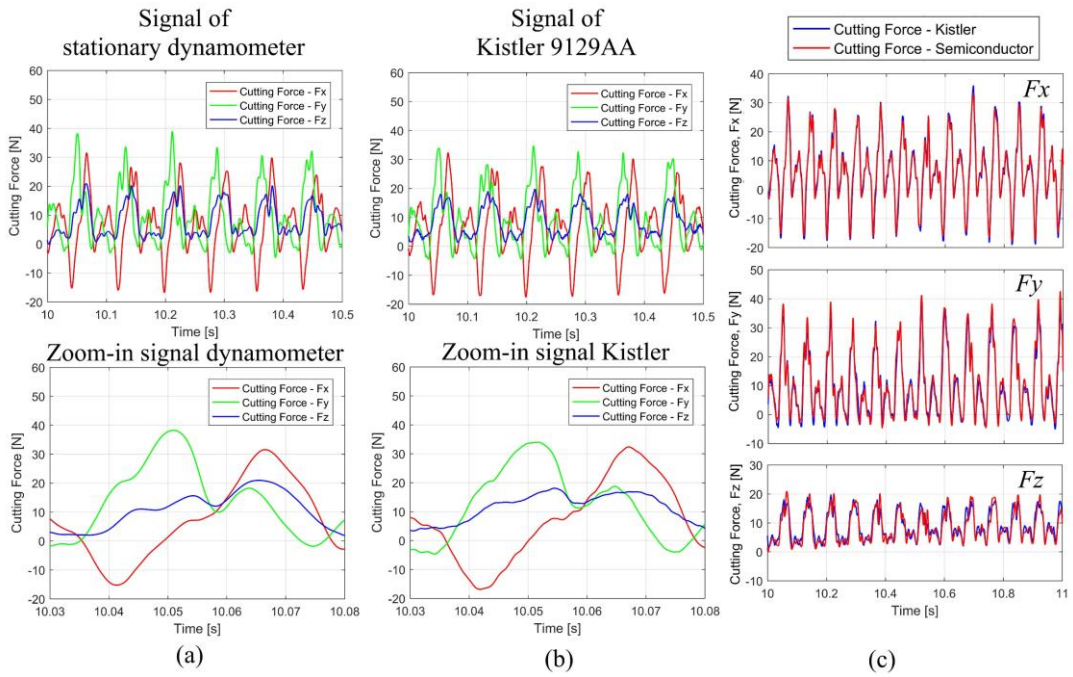

Fig. 20. Cutting force of slot-milling operation: (a) signal from the developed dynamometer; (b) signal from Kistler dynamometer; (c) comparison of cutting force on each channel

Figures 20a and 20b show cutting force signal readings from a slot milling operation taken by a stationary dynamometer and a Kistler dynamometer at the same time. The cutting force signals from the two compared dynamometers were in good agreement in all force directions, especially when the signal for a single rotation of the cutting tool displayed the same pattern. The measurements from the two dynamometers produced the same pattern, and the magnitudes were not significantly different, as shown in Fig. 20c. The action of the cutting tool during engagement with the entrance and exit of the workpiece, generating a random peak pattern by the Kistler dynamometer, may also be detected and followed very well in all

cutting force directions by the stationary dynamometer. This indicated that the custom-designed dynamometer produced readings that were comparable to those obtained by commercially available dynamometers. This demonstrated that the stationary dynamometer, by utilizing four optimized cross-beam force transducers, successfully shows reliable results and has been validated.

5. CONCLUSION

This work designed, optimized, and manufactured a new cross-beam force transducer for a dynamometer to measure the three cutting force components. This dynamometer was designed as a stationary or table dynamometer with four force transducers and numerous piezoresistive strain sensors. To improve sensitivity and stiffness and minimize the cross-talk error, the response surface method (RSM) was used to optimize the three-dimensional parameters of the force transducer, which were studied using the finite element method. This dynamometer was developed to measure horizontal or vertical cutting forces up to 2000 N. The calibration and actual machining tests were conducted in order to evaluate the performance of the stationary dynamometer. Among its characteristics, the designed dynamometer had good linearity, repeatability, and hysteresis, while being able to accurately detect forces with horizontal and vertical sensitivities of 45 μV/N and 71 μV/N, respectively, and cross-sensitivity errors of less than 1.88%. Dynamic testing results indicate that the x, y, and z natural frequencies of the stationary dynamometer are around 1125, 1120, and 1165 Hz, respectively. The thermal test also confirmed that temperature fluctuations gave small changes in the static force offset. The cutting force that was measured during real machining operations was found to have a response that was highly similar to that of the reference dynamometer that was employed.

ACKNOWLEDGMENT

The authors gratefully acknowledge the support from Universitas Syiah Kuala (Grant No. 176/UN11/SPK/PNBP/2021).

REFERENCES

[1] MADHUSUDANA C.K., KUMAR H., NARENDRANATH S., 2016, *Condition Monitoring of Face Milling Tool Using K-Star Algorithm and Histogram Features of Vibration Signal*, Eng. Sci. Technol. an Int. J., 19, 1543–1551.
[2] LIANG Q., ZHANG D., COPPOLA G., MAO J., SUN W., WANG Y., GE Y., 2016, *Design and Analysis of a Sensor System for Cutting Force Measurement in Machining Processes*, Sensors, 16/1, 70.
[3] WOJCIECHOWSKI S., MARUDA R.W., BARRANS S., NIESLONY P., KROLCZYK G.M., 2017, *Optimisation of Machining Parameters During Ball and Milling of Hardened Steel with Various Surface Inclinations*, Measurement, 111, 18–28.
[4] NATH C., BROOKS Z., KURFESS T.R., 2015, *Machinability Study and Process Optimization in Face Milling of Some Super Alloys with Indexable Copy Face Mill Inserts*, J. Manuf. Process., 20, 88–97.
[5] RIZAL M., GHANI J.A., NUAWI M.Z., HARON C.H.C., 2017, *Cutting Tool Wear Classification and Detection Using Multi-Sensor Signals and Mahalanobis-Taguchi System*, Wear, 376–377, 1759–1765.

[6] HUANG P.B., MA C., KUO C., 2015, *A PNN Self-Learning Tool Breakage Detection System in end Milling Operations*, Appl. Soft Comput. J., 37, 114–124.
[7] WANG B., LIU Z., 2016, *Cutting Performance of Solid Ceramic end Milling Tools in Machining Hardened AISI H13 Steel*, Int. J. Refract. Met. Hard Mater., 55, 24–32.
[8] RIZAL M., GHANI J.A., NUAWI M.Z., HARON C.H.C., 2018, *An Embedded Multi-Sensor System on the Rotating Dynamometer for Real-Time Condition Monitoring in Milling*, Int. J. Adv. Manuf. Technol., 95, 811–823.
[9] ZHANG S., LI J.F., WANG Y.W., 2012, *Tool Life and Cutting Forces in end Milling Inconel 718 Under Dry and Minimum Quantity Cooling Lubrication Cutting Conditions*, J. Clean. Prod., 32, 81–87.
[10] AHMADI K., 2017, *Analytical Investigation of Machining Chatter by Considering the Nonlinearity of Process Damping*, J. Sound Vib., 393, 252–262.
[11] BYRNE G., O'DONNELL G.E., 2007, *An Integrated Force Sensor Solution for Process Monitoring of Drilling Operations*, CIRP Ann., 56, 89–92.
[12] TOTIS G., WIRTZ G., SORTINO M., VESELOVAC D., KULJANIC E., KLOCKE F., 2014, *Development of a Dynamometer for Measuring Individual Cutting Edge Forces in Face Milling*, Mech. Syst. Signal Process., 24, 1844–1857.
[13] QIN Y., ZHAO Y., LI, Y., ZHAO Y., WANG P., 2017, *A Novel Dynamometer for Monitoring Milling Process*, Int. J. Adv. Manuf. Technol. 92, 2535–2543.
[14] XIE Z., LU Y., LI J., 2017, *Development and Testing of an Integrated Smart Tool Holder for Four-Component Cutting Force Measurement*, Mech. Syst. Signal Process., 93, 225–240.
[15] LIU M., BING J., XIAO L., YUN K., WAN L., 2018, *Development and Testing of an Integrated Rotating Dynamometer Based on Fibber Bragg Grating for Four-Component Cutting Force Measurement*, Sensors, 18, 1254.
[16] LUO M., LUO H., AXINTE D., LIU D., MEI J., LIAO Z., 2018, *A Wireless Instrumented Milling Cutter System with Embedded PVDF Sensors*, Mech. Syst. Signal Process., 110, 556–568.
[17] DINI G., TOGNAZZI F., 2007, *Tool Condition Monitoring in end Milling Using a Torque-Based Sensorized Toolholder*, Proc. Inst. Mech. Eng., Part B, J. Eng. Manuf., 221, 11–23.
[18] RIZAL M., GHANI J.A., NUAWI M.Z., HARON C.H.C., 2015, *Development and Testing of an Integrated Rotating Dynamometer on Tool Holder for Milling Process*, Mech. Syst. Signal Process., 52–53, 559–576.
[19] QIN Y., WANG D., YANG Y., 2020, *Integrated Cutting Force Measurement System Based on MEMS Sensor for Monitoring Milling Process*, Microsyst. Technol., 26, 2095–2104.
[20] TOTIS G., ADAMS O., SORTINO M., VESELOVAC D., KLOCKE F., 2014, *Development of an Innovative Plate Dynamometer for Advanced Milling and Drilling Applications*, Measurement, 49, 164–181.
[21] SUBASI O., YAZGI S.G., LAZOGLU I., 2018, *A Novel Triaxial Optoelectronic Based Dynamometer for Machining Processes*, Sensors Actuators, A Phys., 279, 168–177.
[22] GOMEZ M., SCHMITZ T., 2020, *Low-Cost, Constrained-Motion Dynamometer for Milling Force Measurement*, Manuf. Lett., 25, 34–39.
[23] SANDWELL A., LEE J., PARK C., PARK S.S., 2020, *Novel Multi-Degrees of Freedom Optical Table Dynamometer for Force Measurements*, Sensors Actuators A. Phys., 303, 111688.
[24] LI Y., ZHAO Y., FEI J., QIN Y., ZHAO Y., CAI A., GAO S., 2017, *Design and Development of a Three-Component Force Sensor for Milling Process Monitoring*, Sensors, 17, 1–18.
[25] YALDIZ S., UNSAÇAR F., SAGLAM H., ISIK H., 2007, *Design, Development and Testing of a Four-Component Milling Dynamometer for the Measurement of Cutting Force and Torque*, Mech. Syst. Signal Process., 21, 1499–1511.
[26] MOHANRAJ T., SHANKAR S., RAJASEKAR R., UDDIN M.S., 2020, *Design, Development, Calibration, and Testing of Indigenously Developed Strain Gauge Based Dynamometer for Cutting Force Measurement in the Milling Process*, J. Mech. Eng. Sci., 14, 6594–6609.
[27] ALIPANAHI A., MAHBOUBKHAH M., BARARI A., 2022, *Cross-Sensitivity Control in a Novel Four-Component Milling Dynamometer for Simultaneous Measurement of Tri-Axial Forces and Torque*, Measurement, 191, 110788.
[28] FIORILLO A.S., CRITELLO C.D., PULLANO S.A., 2018, *Theory, Technology and Applications of Piezoresistive Sensors: A review*, Sensors Actuators A. Phys., 281, 156–175.
[29] LI X., HE H., MA H., 2019, *Structure Design of Six-Component Strain-Gauge-Based Transducer for Minimum Cross-Interference via Hybrid Optimization Methods*, Struct. Multidiscip. Optim., 60, 301–314.
[30] LYU Y., JAMIL M., HE N., GUPTA M.K., 2021, *Development and Testing of a High-Frequency Dynamometer for High-Speed Milling Process*, Machines, 9, 11.